Atmos. Chem. Phys. Discuss., 15, 12539–12582, 2015
www.atmos-chem-phys-discuss.net/15/12539/2015/
doi:10.5194/acpd-15-12539-2015

Atmospheric Chemistry and Physics Discussions

Seasonal trends in black carbon properties and co-pollutants in Mexico City

A. Retama[1], D. Baumgardner[2], G. B. Raga[3], G. R. McMeeking[2], and J. W. Walker[2]

[1]Dirección de Monitoreo Atmosférico, Secretaría del Medio Ambiente, Mexico City, Mexico
[2]Droplet Measurement Technologies, Boulder, CO, USA
[3]Centro de Ciencias de la Atmósfera, Universidad Nacional Autónoma de México, Ciudad Universitaria, México

Received: 24 February 2015 – Accepted: 13 April 2015 – Published: 29 April 2015

Correspondence to: D. Baumgardner (darrel.baumgardner@gmail.com) and G. R. McMeeking (gavin@dropletmeasurement.com)

Published by Copernicus Publications on behalf of the European Geosciences Union.

Abstract

The Mexico City Metropolitan Area (MCMA) is a region that continues to grow in population and vehicular traffic as well as being the largest source of short lived climate pollutants (SLCP) in Latin America. The local city government has made significant progress in controlling some of these pollutants, i.e. ozone (O_3) and carbon monoxide (CO), but particulate matter ($PM_{2.5}$ and PM_{10}) and black carbon (BC) have shown little response to mitigation strategies that have been in place for more than two decades. For the first time, extended measurements have been made of equivalent black carbon (eBC), derived from light absorption measurements made with a Photoacoustic Extinctiometer (PAX), over a 13 month period from March 2013 through March 2014. The daily trends in workday (Monday through Saturday) and Sunday eBC, $PM_{2.5}$ and the co-pollutants CO, O_3 and NO_x are evaluated with respect to the three primary seasons in that region: rainy, cold-dry and warm-dry.

The maximum values in all of the particle and gas concentrations were significantly larger (Student's t test, $P < 0.05$) during the dry periods than in the rainy season. The changes from rainy to dry seasons for eBC, $PM_{2.5}$, CO, O_3, and NO_x were 8.8 to 13.1 $\mu g\,m^{-3}$ (40 %), 49 to 73 $\mu g\,m^{-3}$ (40 %), 2.5 to 3.8 ppm (40 %), 73 to 100 ppb (30 %) and 144 to 252 ppb (53 %), respectively.

The primary factors that lead to these large changes between the wet and dry seasons are the accelerated vertical mixing of boundary layer and free tropospheric air by the formation of clouds that dilutes the concentration of the SLCPs and the decreased actinic flux that reduces the production of ozone by photochemical reactions.

A significant "weekend effect" was also identified, particularly the decrease in BC due to fewer large transport vehicles that are fueled by diesel that produces a large fraction of the BC emissions. The other co-pollutant concentrations are also significantly less on weekends except for O_3 that shows no change in maximum values from workday to Sunday. As has been noted in previous studies, this lack of change is a result of the

ACPD
15, 12539–12582, 2015

balancing effects of lower precursor gases, i.e. VOCs, offset by lower NO_x that is an O_3 inhibitor.

A comparison of average, maximum values of eBC measured during the one year period of the current study with maximum values measured in short field campaigns in 2000 and 2006 show that there has been no significant change in the eBC emissions over a 14 year period. This suggests that the current pollution mitigation strategy will need to be evaluated to develop new methods than can decrease potentially toxic levels of this particulate pollutant.

1 Background

Short-lived climate pollutants (SLCP) are those gases and particles whose atmospheric lifetimes range from less than a day to a few years (Shindell et al., 2012; Bowerman et al., 2013) and exert a positive radiative forcing to the global climate. These pollutants, black carbon (BC), methane (CH_4), tropospheric ozone (O_3) and selected hydrofluorocarbons (HFCs) also impact the environment and have negative effects on human health. Although these pollutants play a role in the radiative balance of the earth and have global impacts, their more immediate effects are observed locally and regionally.

Black carbon has been identified as the atmospheric component whose regional warming effect on climate is second only to carbon dioxide (Bond et al., 2013). Unlike CO_2 whose increasing global concentrations and long lifetime require an international scale effort to reduce concentrations, BC is a contaminant whose negative effects locally could be significantly decreased through local and regional mitigation measures (Shindell et al., 2012; Bowerman et al., 2013). This is an optimistic possibility since BC is a product of inefficient combustion from diesel motor vehicles (cars, buses, and trucks), commercial processes (e.g. brick making, cooking, oil and gas production), residential heating and cooking and open biomass burning (e.g. agricultural clearing and inadvertent forest fires). All of these emission sources lend themselves to a greater

ACPD
15, 12539–12582, 2015

level of control through regulatory actions and with technologies that are already available. Likewise, the other co-pollutant SLCPs may be similarly reduced through the measures taken to reduce BC.

The Mexico City Metropolitan Area (MCMA), referred to as Greater Mexico City, has a population that now exceeds 22 million people according to the 2014 census, making it the largest urban area in North America. The MCMA is also one of the most polluted megacities in the western hemisphere and a major source of SLCPs that not only affect the local and regional environment but can also contribute to global climate change (Barth and Church,1999; Singh et al., 2009). According to the most recent assessment by the city government (SMA-GDF, 2012) annual emissions of BC, $PM_{2.5}$, CO and NO_x are 2, 9.4, 1606 and 239 kilotons (Kt), respectively.

The Mexico City government established a network of automatic air quality stations in 1986 (Red Automática de Monitoreo Atmosférico – RAMA, http://www.aire.df.gob.mx/) to monitor O_3, CO, NO_x and SO_2, adding mass concentration of particles with aerodynamic diameter less than 10 µm (PM_{10}) in 1991 and and less than 2.5 µm ($PM_{2.5}$) in 2003. RAMA currently has 29 stations located in the MCMA (Fig. 1, courtesy of the city government's environmental agency, http://www.aire.df.gob.mx/default.php). Until recently, however, there were no measurements of BC at any of the RAMA stations. The few BC measurements previously available had been taken during short field campaigns. The first published data on BC were by Baumgardner et al. (2000) who analyzed measurements with a Particle Soot Aerosol Photometer (PSAP) to derive equivalent black carbon (eBC), the name that has been given to BC derived with filter techniques (Petzold et al., 2013). These measurements were made during a two week period in November 1997 at an elevated site (400 m above the city) in the southwest sector of Mexico City. Additional measurements were made, also with a PSAP, at three RAMA sites in 2000 over a three week period in January and February (Baumgardner et al., 2002). In the spring of 2003 and again in 2005, measurements were made with a co-located PSAP and a single particle soot photometer (SP2)(Baumgardner et al., 2007). These were very short measurement campaigns of one week each. In 2003,

ACPD
15, 12539–12582, 2015

as part of the MCMA-2003 campaign (Molina et al., 2007), a mobile laboratory was deployed at various locations around the city. Filter samples were evaluated with electron microscopy and aerosol mass spectrometry (Johnson et al., 2007) and eBC was derived from an aethalometer, a filter based instrument like the PSAP (Jiang et al., 2005). Marley et al. (2007) also made measurements of eBC during MCMA-2003 with an aethalometer and compared them with measurements that they had made in 1997.

During the MILAGRO campaign in March 2006 (Molina et al., 2010), measurements of eBC and elemental carbon (EC) were made at various locations within the city (Marley, 2009a, b) and in the regions around the urban area (Baumgardner et al., 2009; Subramanian, 2010).

In 2011, a new instrument, the Photoacoustic Extinctiometer (PAX) was installed at the RAMA supersite located in the north central section of the city (Fig. 1). From 2011 to 2013 the instrument was being evaluated as a possible addition to the RAMA air quality network. In March 2013, the PAX was certified as an operational instrument for measuring the optical properties of BC relevant for climate, i.e. the light scattering and absorption coefficients, B_{scat} and B_{abs}, and the derived eBC. We report in this paper the results from a year of continuous observations made by this instrument since March 2013.

Numerous studies have focused on a better understanding of the meteorological processes that transport pollutants from Mexico City and the chemical processes that lead to the production of ozone and aerosol particle mass (e.g. Stephens et al., 2008; Molina et al., 2010 and references therein). There have been no studies, however, that look at how the chemical processes are linked to the seasonal meteorology. The objective of this study is to evaluate the temporal trends in some of the SLCPs (BC and O_3) and related co-pollutants (CO, NO_x and $PM_{2.5}$) and show how they are modulated by seasonal variations in precipitation and radiation.

This study is an extension of the evaluation of Mexico City pollutants by Stephans et al. (2008) who analyzed daily trends but did not have information on BC. In the following analysis, the daily trends in the concentrations of SLCPs over a 13 month period

ACPD
15, 12539–12582, 2015

are compared with respect to seasonal climate changes and linked to the underlying physical processes that lead to seasonal differences.

2 Measurement methodology

The RAMA "super-site" (Fig. 1) is located in an area of the city that is mixture of private residences and industry (19°29.0′ N, 99°9.85′ W, and 2243 m altitude). The site is located approximately 300 m from a major highway that is a conduit for traffic to/from the north. Automobiles, local and regional buses and heavy trucks are responsible for most of the primary pollutants (CO, NO_x, BC and primary $PM_{2.5}$). The cars and buses run primarily on unleaded gasoline whereas the trucks mostly consume diesel. Hence, the majority of the BC comes from the trucks but, by the time the air reaches the measurement site, the BC is well mixed with the CO and NO_x that are primarily produced by the cars and buses.

2.1 Meteorology, radiation, gas and $PM_{2.5}$ measurements

Temperature and relative humidity were measured using a Met One (Met One Instrument, Grants Pass, OR) model 083E sensor located inside an aspirated radiation shield. Wind speed and direction were measured with a Met One model 010C lightweight three-cup anemometer, and a Met One model 020C lightweight airfoil vane. The temperature and relative humidity sensors were positioned in a meteorological tower 4 m above the ground. The anemometer and vane were positioned at the top of the 10 m meteorological tower. All sensors were calibrated annually. The ultraviolet radiation, over the wavelength range from 400–320 nm (UV-A), was measured with a Solar Light UVA model 501 radiometer that outputs its data in mW cm^{-2}. The UV-A measurements used in this paper were not made at the "Supersite", but are an average from six stations across the city (see Fig. 1): Merced (MER), Montecillo (MON), Pedregal (PED), San Agustin, (SAG), Santa Fe (SFE), and Tlalnepantla (TLA).

ACPD
15, 12539–12582, 2015

Ozone was measured by ultraviolet photometry (Teledyne API model 400E, San Diego CA). NO_x, defined operationally, was measured by chemiluminescence following conversion in a heated molybdenum NO_2-to-NO converter (Teledyne-API model 200E, San Diego, CA). CO was measured by a gas filter correlation, non-dispersive infrared analyzer (Teledyne API model 300E, San Diego, CA). The gas analyzers were tested every two weeks with a known standard and calibrated quarterly.

$PM_{2.5}$ was measured with a TEOM 1400A ambient particulate monitor 8500C FDMS (Thermo Scientific, Franklin, MA), with a BGI VSCC $PM_{2.5}$ cyclone inlet for size selection. $PM_{2.5}$ hourly concentrations are reported at local temperature and pressure conditions. The TEOM is operated at a temperature of 35 °C in order to measure dry particle mass.

2.2 The photoacoustic extinctiometer

The eBC, B_{scat} and B_{abs} are derived from the PAX, a sensor that evolved from the Photoacoustic Soot Spectrometer (PASS) developed at the University of Nevada (e.g., Arnott et al., 2005, 2006; Moosemuller et al., 2009) and commercialized by DMT (Chan et al., 2011; Holder et al., 2014; Liu et al., 2014; Nakayama et al., 2015). The PAX is a single wavelength instrument that performs simultaneous measurements of aerosol scattering and absorption coefficients using a single diode laser modulated at approximately 1500 Hz. Here we describe the 870 nm version, but the 375, 405, and 532 nm versions of the instrument have identical measurement cells and differ only in a few optical components.

Figure 2 shows a diagram of the PAX measurement cells. The nominal 1 LPM sample flow first passes a solenoid pinch valve (not shown) that allows for periodic filtered-air sampling to determine the instrument background signals. The lengths of sample tubing between the filter line and sample line are the same to provide the same acoustic properties along both channels. The sample flow passes into an acoustically insulated enclosure containing the measurement cells, where it is then split, making opposing 90° turns into the scattering and absorption measurement regions. The sample is ex-

ACPD
15, 12539–12582, 2015

hausted through two ports at the ends of the absorption cells before being filtered and pumped out of the instrument. The flows are controlled using critical orifices and do not affect the calculated absorption and scattering coefficients, which depend only on the properties of the sampled particles and geometry of the measurement region. Sample flow does affect the residence time of the sample in the measurement cells, which is approximately 7 s.

The absorption cell includes a 0.635 cm diameter tube 10.8 cm long called the resonator. A small microphone located at the top of the resonator detects the pressure perturbations induced by the heating of the light absorbing particles. The microphone signal is passed through a fast Fourier transform circuit that gives the peak power at the resonator frequency, which is calculated based on the resonator geometry and air pressure, temperature and dew point temperature measured in the cell. The microphone raw pressure signal (p_{mic}) is converted to the raw light absorption coefficient using Eq. (1):

$$b_{\mathrm{abs,\,raw}} = \frac{p_{\mathrm{mic}} A \pi^2 f}{P_{\mathrm{L}} (\gamma - 1) Q} \cos \phi_{\mathrm{raw}} \quad (1)$$

where A is the resonator cross-section, f is the calculated resonator frequency, P_{L} is the laser power, γ is the ratio of isobaric and isochoric specific heat for air, Q is the calculated resonator quality factor (also calculated from measured cell pressure, temperature and dew point temperature), and ϕ_{raw} is the phase raw absorption signal relative to the phase of the laser power signal plus the phase correction. The phase correction accounts for the difference between the speed of light and sound that translates to a phase shift in the acoustic pressure measured by the microphone relative to the modulated laser power incident on the absorbing material. See Arnott et al. (2005) for more details on applying phase corrections to photoacoustic measurements of light absorption coefficients.

The raw absorption and scattering signals must be corrected for background absorption and scattering in the cell to give the desired light absorption and scatter-

ACPD
15, 12539–12582, 2015

ing coefficients due to the sampled aerosol particles. Background absorption arises from absorbing gases (not important for the 870 nm version of the PAX but relevant for shorter wavelength versions), absorption by the cell and particles deposited to the cell surfaces (especially the cell windows) and acoustic and electrical noise that contributes to signal at the resonator frequency. The background scattering is not sensitive to acoustical noise, but is affected by electrical noise and light scattering from the cell surfaces and particles deposited to the cell surfaces and windows. The background signals are measured simultaneously at a user-specified interval, typically once every ten minutes, by passing the sample air through a filter before it enters the measurement cell. The background measurement period occurs after a 20 s flush with particle-free air to mix sampled particles out of the measurement cells and lasts 30 s, followed by another 20 s flush before regular measurements resume. Background absorption and scattering values are saved in the data record and automatically subtracted from the measured raw signals to give the absorption and scattering coefficients in real-time. Typically the background drift is small ($< 3\,Mm^{-1}$) compared to the observed scattering and absorption coefficients, especially in more polluted environments like Mexico City. Background drift occurs due to small changes in sampling environment, such as temperature and relative humidity. Over longer periods of time backgrounds are affected by contamination on the cell windows and minor changes in the optical alignment. Cleaning and re-alignment of the system can be necessary when the magnitude of the background drift becomes comparable to changes in the scattering and absorption values on the timescales of the filtered background measurements. Post-processing of background values to apply a linearly-interpolated correction (using background measurements before and after a sample point) provides a better correction for background drift compared to the standard background correction performed in real-time by the instrument.

The PAX absorption and scattering sensitivity depends on the sampling conditions and laser power in the cell. The laser power in turn depends on the quality of the alignment and level of contamination on the cell windows. The scattering sensitivity is

ACPD
15, 12539–12582, 2015

mainly limited by the small measurement volume and variability in the particle sample stream. The absorption sensitivity is mainly limited by electrical and acoustical noise that cannot be distinguished from the true particle signal. While noise in the sampling environment can reach the acoustic cell through vibrations in the case, a bigger factor is acoustical noise transmitted through the sampling line directly into the resonator. Helmoltz notch filters can be inserted into the sampling line to filter noise at the measurement frequency in environments with high acoustic noise and relatively low aerosol loadings. In Mexico City, the PAX was installed in a temperature and noise controlled environment with minimal acoustic noise.

Figure 3 shows the corrected absorption coefficients and Allan variance plot for the absorption signal measured during overnight sampling of filtered air with an 870 nm PAX. The instrument performed a background measurement approximately every 10 min, which corrected for the instrument drift on timescales longer than 10 min, so the variance is only shown up to a five-minute averaging interval. At the highest temporal resolution, 1 s, the variance was 0.14 Mm^{-1}, equivalent to about 30 $ng\,m^{-3}$ black carbon using the factory applied mass-specific absorption cross-section (MAC) of 4.74 $m^2\,g^{-1}$ at 870 nm (Bond and Bergstrom, 2006). The three-sigma sensitivity for 1 s averaging was 1.1 Mm^{-1} (0.23 $\mu g\,m^{-3}$ BC). The values are a "best case" scenario where the environmental conditions were very stable (running overnight in an empty laboratory) and because the particle filter also acted to block acoustical noise from the sampling environment from reaching the cell. We have observed 1 s variance in PAX absorption signals of $\sim$ 1–5 Mm^{-1} depending on sample environment.

The PAX uses a wide-angle (6–174°) integrating reciprocal nephelometer to measure the light scattering coefficient. The scattering detector consists of a Teflon diffuser placed in front of a photodiode (see Fig. 2). The scattering measurement responds to all particle types regardless of chemical makeup, mixing state, or morphology.

The PAX is calibrated through a two-step process by first introducing high concentrations of purely light scattering particles followed by high concentrations of partially absorbing particles to the measurement cells (Arnott et al., 2000). The concentrations

ACPD
15, 12539–12582, 2015

must be high enough to allow direct measurement of the extinction coefficient (b_{ext}) from the measured reduction in laser power using Beers law:

$$b_{ext} = -\frac{1}{l} \ln \frac{I}{I_0} 10^6 \, [\mathrm{Mm}^{-1}] \quad (2)$$

where I is the average laser power measured when the high concentration of particles is being sampled, I_0 is the average laser power immediately before and after the high concentrations are introduced to the cell, and l is the path length of the laser beam through the entire optical cavity (scattering region and absorption region) between the two windows, which for the PAX is 0.354 m.

Ignoring truncation in the nephelometer cell, an error that is of order 4 %, the measured extinction coefficient equals the measured scattering coefficient for purely scattering particles (e.g, nebulized, dry ammonium sulfate). The relationship between the measured extinction and scattering coefficients are fit using a linear regression giving a calibration factor for the scattering measurement. Introducing calibration particles that have non-zero absorption means the measured extinction equals the now-calibrated scattering coefficient plus the measured calibration coefficient. Subtracting the measured scattering coefficient from the extinction coefficient determined from Beers law gives the absorption coefficient, which can be regressed against the measured absorption coefficient to obtain a second calibration factor for the absorption cell. One major uncertainty introduced by this method of calibration is it assumes the measured particles have similar scattering phase functions so the truncation error in the scattering cell cancels.

The PAX measures the light scattering and absorption coefficients, B_{scat} and B_{abs}, directly using the in-line nephelometer and photoacoustic technique, respectively. The single scattering albedo (SSA), defined as the ratio of B_{scat} to the sum of B_{scat} and B_{abs} (extinction coefficient) is also derived and recorded, along with the eBC that is derived from B_{abs} using the MAC of 4.74 $\mathrm{m}^2\,\mathrm{g}^{-1}$ at 870 nm (Bond and Bergstrom, 2006).

The PAX was operated with a $PM_{2.5}$ cyclone particle separator on the inlet in order to remove larger particles and the particle stream was also dried using a diffusion drier

ACPD
15, 12539–12582, 2015

in order to minimize measurement effects at high relative humidity (e.g., Lewis et al., 2009; Murphy et al., 2009) and also to provide the scattering coefficients of dry particles only.

The uncertainty in the measured B_{scat} is ca. ±10 % due to the accuracy with which the instrument can be calibrated, the truncation error, and aerodynamic losses in the inlet system that brings the ambient air into the sample cavity. The uncertainty in the measured B_{abs} is ca. ±20 %. This uncertainty stems primarily from the accuracy of the calibration but the losses in the inlet system also contribute to the overall accuracy. The accuracy of the derived eBC is estimated to be on the order of 20–30 % and depends a lot on the composition of the BC (Bond and Bergstrom, 2006). The conversion from B_{abs} to eBC uses the mass absorption coefficient that is sensitive to the size distribution of the BC as well as the amount of non-absorbing material that may encapsulate it. Using different mixing rules, Bond et al. (2007) arrived at an average enhancements in B_{abs} of 1.5; hence, the derived concentrations may be as much as 50 % higher than the actual concentration of BC due to this coating effect.

3 Measurements and analysis

The meteorology, gas and particle measurements were made at the RAMA supersite from 6 March 2013 to 31 March 2014. Mexico City is located in a sub-tropical zone where the seasons can be generally separated into three periods: (1) the rainy season extends from June until October with an average annual rainfall of about 600 mm, (2) the cool, dry season, from November to March and (3) the warm-dry period from April through May. The starting and ending dates for these seasons will vary from year to year but these three seasonal periods will be used in the analysis as an operational definition. During the dry months, clear sky conditions lead to a strong thermal inversion at night (Collins and Scott, 1993). This persists until several hours after sunrise when it is eroded by turbulent mixing, generated by strong solar heating of the surface.

ACPD
15, 12539–12582, 2015

During the rainy season, the interaction of the predominant easterly winds with the mountains that surround the Mexico City basin force upward motions and convection. Early mornings are typically clear during this season, but thermal inversions are infrequent due to the high moisture content in the atmosphere. Solar heating during the mornings leads to the development of turbulent eddies that vertically mix the pollutants emitted at the surface. Convection develops over the mountains, resulting in further dilution of pollutants due to the vertical updrafts within clouds. The precipitation that develops from the convective clouds has a large gradient within the basin (Jáuregui, 1971), from around 400 mm yr^{-1} in the northeast to almost 1200 mm yr^{-1} in the southwestern part of the city.

The concentration of gases and aerosols within the boundary layer is controlled by the balance between the emission rates of primary pollutants (i.e. CO, NO_x, volatile organic compounds (VOC) and eBC), the rate of secondary production due to photochemical reactions of O_3 and $PM_{2.5}$, and the rate of dilution by mixing with tropospheric air. Not only does this balance vary with the season, but because the emissions patterns change from the workdays (Monday through Saturday) to Sunday, we would expect to observe differences in the trends of SLCP when comparing these two seasons.

3.1 Seasonal trends

The average, median, daily average maxima and the quantiles values at 5, 25, 75 and 95 % were calculated for CO, NO_x and O_3 and are shown in Fig. 4a–c by season, workdays and Sundays. The box and whisker plots show median (horizontal line within the box), 25 % quantile (bottom of box), 75 % quantile (top of box), 5 % quantile (bottom whisker) and 95 % quantile (top whisker). In addition the average of the daily maxima are shown with the red, filled circles. The same information for eBC, $PM_{2.5}$, B_{scat} and SSA is shown in Fig. 5a–d, respectively. The values used to generate these graphs are tabulated in Table 1.

Table 2 summarizes the average and standard deviations about the average, maximum daily values (with the exception of the SSA that is the average, not the average

ACPD
15, 12539–12582, 2015

maxima), tabulated by season, workdays and Sundays. A Student's t test was applied to the differences and the significance evaluated at a confidence level of $P < 0.10$, i.e. that there is less than a 10 % probability that the observed differences are due to chance. For each season and each measured parameter the significance of the differences between the workday and Sunday values was tested using the hypothesis that the average values were from the same population. This hypothesis was rejected when the value of $T > |1.7|$, the critical value for $P < 0.10$ with the pooled degrees of freedom of the two samples in each comparison. In the Table, underlined, non-bold numbers had Sunday values significantly smaller than the workdays, i.e. the null hypothesis that they were from the same population was rejected. Likewise, the underlined, bold numbers are the case where the Sunday value exceeded the workday value.

Using the same approach the difference in the average maximum values between each of the three seasons was tested (last three columns in Table 2). The non-bold numbers in italics indicate a significant decrease in a parameter value from one season to the next and the bold numbers in italics highlight significant increases. The value in each of these cells is the computed value of the t statistic.

Median concentrations of CO and NO_x (Fig. 4a and b, respectively) do not significantly change with season, whereas there is a clear increase in O_3 (Fig. 4c) during the warm-dry season compared to either the rainy or cold-dry season. The maximum concentrations for all three of the gases increase significantly (Table 2) in the dry seasons (cold and warm) compared to the rainy season. This increase is seen for workdays as well as Sundays. A significant increase from the cold-dry to the warm-dry season is only observed in the O_3 concentrations, due to the larger actinic flux late in the spring. Of note is that the maximum CO concentrations on Sundays actually decrease between the cold and warm season (green shaded box in Table 2).

A "weekend effect" is observed for CO, NO_x and O_3. The maximum NO_x concentrations decrease between workdays and Sundays by more than 50 % during all three seasons whereas the maxima CO decreases significantly from workdays to Sundays only during the rainy and warm-dry seasons (Table 2). As discussed by Stephens

ACPD
15, 12539–12582, 2015

et al. (2008). The lack of a decrease on Sundays is a "weekend effect" because with the decrease in VOCs (CO is a surrogate for VOCs), the O_3 was expected to decrease as well. As detailed by Stephens et al. (2008) for Mexico City in particular, there are several possible mechanisms responsible for this behavior; however, the one that is most plausible (Stephens et al., 2008) is related to the inhibition of O_3 by NO_x under VOC-limited condition. The production of O_3 is positively correlated with VOC emissions and negatively correlated with NO_x. Since the CO (VOC) and NO_x are both decreasing, there is a balancing effect on O_3 production, i.e. less production from VOC reaction but les inhibition from NO_x.

Figure 5a and b displays the same grouping of comparisons as Fig. 4 but for the mass concentrations of $PM_{2.5}$ and eBC. The median $PM_{2.5}$ concentrations increase between rainy and cold-dry and between cold-dry and warm-dry. In contrast, the median concentration of eBC does not show a seasonal trend. When evaluating the seasonal trends of the maximum concentrations, both the $PM_{2.5}$ and eBC have much larger values in the dry seasons than during the rainy season; however, unlike the $PM_{2.5}$ that also shows a significant increase between the cold and warm seasons, the eBC actually decreases slightly between these two seasons, but not significantly (Table 2). There is a clear "weekend effect" that is seen in the maximum concentrations drawn in Fig. 5, and highlighted in Table 2. The concentrations decrease from the workdays to Sundays over all seasons; however, unlike the eBC whose decreases are statistically significant over all seasons, the $PM_{2.5}$ decreases are only significant during the rainy and cold-dry seasons.

The seasonal impacts on the optical properties of the aerosol particles are illustrated in Fig. 5c and d that show the scattering coefficient, B_{scat}, and SSA, respectively. Note that the SSA is only reported as the average daily and not a maximum. Although the figures suggest that the differences between seasons of B_{scat} and SSA are small, as seen in Table 2, there are statistically quantifiable differences, although for B_{scat}, only the increase from rainy to warm-dry is significant. The SSA values are much more sensitive to season, even though the average values do not appear that different. The

ACPD
15, 12539–12582, 2015

SSA decreases from the rainy to cold-dry season but increases from the cold-dry to warm-dry seasons. A decrease in SSA indicates that there is proportionally more light absorption than scattering, whereas an increase in SSA suggests the opposite trend. Since the B_{scat} is seen to be relatively insensitive to seasonal changes, the changes with SSA are primarily a result of the seasonal sensitivity of Babs, i.e. changes in the eBC.

3.2 Daily trends

An examination of the average, hourly properties of the pollutants, differentiated by season and by workday/Sunday, provides a different perspective than the comparison of just the daily quantiles and maxima that are shown in Figs. 4 and 5. All of the pollutants have daily cycles that are linked to the traffic patterns, photochemical processes and boundary layer depth (vertical mixing with clean air). Figure 6a–c illustrates these cycles for CO, NO_x and O_3, respectively. The solid and dashed lines separate the measurements into the workdays (Monday–Saturday) and Sunday. The red, green and blue curves differentiate the trends by season: warm-dry, rainy and cold-dry, respectively.

The average hourly CO and NO_x (Fig. 6a and b) have very similar patterns over all three seasons. The maximum concentrations are reached between 07:00 and 08:00 LST during the rainy and warm-dry seasons and between 08:00 and 09:00 in the cold-dry seasons, respectively. A secondary, broader maximum is seen near midnight, formed after the concentrations begin increasing after their minimum at 16:00. As was illustrated in Fig. 4a and b, the maximum CO and NO_x values during the rainy season are c.a. 40 % lower than the dry seasons; however, when comparing the rainy season with the warm-dry season, this difference appears to be dominant only from about 4:00 to 11:00 LST. Outside of this time period the concentrations are nearly the same. Likewise, after 13:00 LST there is no longer a significant difference in the CO and NO_x concentrations in the rainy and cold-dry seasons. This is a result of the manner in which the vertical mixing progresses and the boundary layer depth increases during the three seasons. The shift in the time of the peaks between the cold-dry and

ACPD
15, 12539–12582, 2015

other seasons is due to the shift from daylight savings time (DST) the first Sunday in November then back the first Sunday in April. This is just a virtual shift because the measurement time base does not shift with changes in DST.

In the rainy season, as discussed previously, the boundary layer growth is accelerated by the vertical motions as convective clouds develop, resulting in much larger updrafts that reach higher in the troposphere than during the dry season. This leads to more rapid dilution of the primary emissions. At the same time, the clouds reduce the solar radiation and limit the photochemical reactions that produce O_3. In the dry seasons there is also vertical mixing but not as intense as during the rainy season and it is only due to dry turbulent eddies within the boundary layer that slowly erode the inversion at the top by mixing with the free tropospheric air. There is less O_3 during the dry-cold period because the solar zenith angle is larger with subsequent decreased photochemical activity.

The minimum at 16:00 LST, and steady increase thereafter, is due to the maximum in the boundary layer depth in late afternoon (Stull, 1988; Perez-Vidal and Raga, 1997), followed by its gradual collapse as the solar insolation diminishes and the dilution decreases while the daytime primary emissions remain more or less constant. There is actually an increase in emissions from traffic during the evening rush hour in Mexico City that contributes to the increase in CO and NO_x at night (Edgerton et al., 1997; Shifter et al., 2003).

A "weekend effect" (only Sunday) is also evident during all seasons whereby the maximum concentrations on Sundays are 50–70 % lower than on workdays (see Table 2) regardless of the time of day. Given that the meteorology on Sundays is not expected to differ from workdays, i.e. the boundary layer depth and solar radiation should not be dependent on the day of the week, this decrease over all seasons must be due to decreased, work-related traffic on Sundays.

The hourly average O_3 (Fig. 6c) reaches the maximum concentrations between 13:00 and 14:00 LST during the rainy season and between 14:00 and 15:00 LST during the dry periods. Differences in the O_3 concentrations between the rainy and cold-dry

ACPD
15, 12539–12582, 2015

seasons are only obvious between the hours of approximately 14:00 and 20:00 LST and between 10:00 and midnight LST when comparing the rainy and warm-dry periods. Unlike the seasonal differences that are observed with the CO and NO_x concentrations, the differences in O_3 are primarily being driven by the photochemical production of O_3. As summarized in Table 1, the cold-dry season maximum O_3, is 13 % larger than the rainy season whereas the maximum during the warm-dry season is 47 % larger. The impact of available solar radiation on the production of O_3 from the precursor gases (NO_x and VOCs) can be better understood by comparing measurements of the UV-A that are shown in Fig. 7a and b. The summer months of June–August are a period with minimum solar zenith angle; yet, as these figures show, both the daily accumulated UV-A (Fig. 7a), and the hourly UV-A (Fig. 7b) are only about 10 % greater than the cold-dry season and 10 % less than during the warm-dry season. Since the precursor gases, represented by the NO_x, are more than 50 % higher in concentration in the dry seasons, the slightly higher number of photons in the rainy season are offset by the larger decreases in the reactive gases due to more vigorous vertical mixing in the presence of clouds.

Figure 8a and b displays the hourly trends in $PM_{2.5}$ and eBC where it is seen that there are large differences, not only in the hourly concentrations that vary with season, but the hours during which these $PM_{2.5}$ mass concentrations peak also change with season, although the eBC to a lesser extent. The differences between the rainy and dry season $PM_{2.5}$ maximum average mass concentrations are 34 and 47 %, respectively, when compared to the cold and warm-dry seasons (Table 2). For the eBC, these differences are 44 and 36 %. Whereas the $PM_{2.5}$ concentrations during the two dry seasons are always larger than those in the rainy season, regardless of the time of day, this is only the same for eBC when comparing the cold-dry to the rainy season. In the case of the warm-dry to rainy season comparison, the eBC concentrations in the warm-dry season only exceed those during the rainy season from approximately midnight until 11:00 LST. After this time the concentrations are on average the same. This is a reflection of the same atmospheric process that was discussed for CO and NO_x,

ACPD
15, 12539–12582, 2015

i.e. the difference in vertical mixing between the rainy and warm-dry seasons. There is much greater dilution of the eBC during the rainy season since clouds are responsible for the vertical mixing.

The daily cycles in $PM_{2.5}$ have seasonal patterns that are much more distinctive than either the gases (Fig. 6a–c) or the eBC. There is a slight shift in the hour of maximum concentrations for the eBC, between 06:00 and 07:00 for the rainy and warm-dry seasons, and between 07:00 and 08:00 for the cold-dry season. This shift is only a result of the change from daylight savings time (DST) in November and April, so that in the cold-dry season the major commuter traffic begins an hour later relative to the clock used on the RAMA data that does not change to DST. The $PM_{2.5}$ reaches maximum concentrations between 07:00 and 08:00, 09:00 and 10:00 and 10:00 and 11:00, respectively for the warm-dry, cold-dry, and rainy seasons. The large shift in the peaks of the daily cycles are the result of both the atmospheric dynamics, i.e. boundary layer growth, and the chemical process behind the formation and growth of the particles that make up the $PM_{2.5}$. This is discussed in more detail in Sect. 3.4.

There is a very distinctive "weekend effect" displayed by the eBC but only the dry-cold season $PM_{2.5}$ concentrations show a similar change. As summarized in Table 2, the maximum eBC concentration decrease by more than 50 % from workdays to Sundays. As can be observed in Fig. 8b, the difference is distinct over all hours of the day but is the most predominant between around 05:00 to 18:00. One of the major differences in primary emissions of BC between the workdays and Sundays is that the use of large, diesel burning trucks and machinery is much less on Sundays. Although vehicular traffic in general is much less on Sundays, since combustion of diesel fuel is the major contributor of BC emissions in the city, the large decrease in BC is linked more to the decrease in diesel combustion than gasoline. To support this assertion, looking only at the dry season to remove any effects of precipitation, the average eBC to CO ratio on workdays was 3.5 $\mu g\,m^{-3}$ of eBC to 1.0 ppm of CO. This compared to the Sunday ratio that is 2.4 $\mu g\,m^{-3}$ of eBC; hence, the eBC decreases by a much larger percentage than the CO.

ACPD
15, 12539–12582, 2015

The hourly trends in the optical properties of the aerosol particles, B_{scat} and SSA, are shown in Fig. 9a and b, respectively. The maximum B_{scat} falls between 09:00 and 10:00 LST during the warm-dry season and between 10:00 and 11:00 LST in the rainy and cold-dry period. Unlike the particle mass concentrations of $PM_{2.5}$ and eBC, there are no distinct differences from season to season in the maximum values. The differences are instead seen in the morning hours before reaching the maximum then again in the afternoon. During both of these periods the dry season values are about 30 % larger than the rainy period. In the same way that the trends in $PM_{2.5}$ are a balance between the processes that drive particle growth and the dynamic processes that dilute the number concentration, likewise the trends in the scattering are driven by complex interactions. The intensity of light scattering and the $PM_{2.5}$ mass concentrations are strongly correlated because both are proportional to particle concentration and size. The B_{scat} and $PM_{2.5}$ values peak at the same time periods during the three seasons (Figs. 8a and 9a).

The SSA reaches its minimum value in the morning between 06:00 and 07:00 LST in the warm-dry and rainy seasons and between 07:00 and 08:00 LST in the cold-dry season. As mentioned previously, the SSA appears to be much more sensitive to changes in eBC, i.e. light absorption, than in B_{scat}. Since the minima in the SSA correspond to the maxima in the eBC, rather than changes in B_{scat}, this further underscores the sensitivity of SSA to changes in the eBC concentration in this environment. The changes with season of the SSA do not mirror those of eBC. Whereas the maximum eBC in the dry seasons was significantly larger than the rainy season (Table 2), the trends in the SSA are more complicated with the rainy and warm-dry season values being nearly equal until they diverge after midday at 13:00 LST with the rainy season SSA decreasing while the warm-dry period maintains an almost constant value. These trends are best understood by comparing the trends in $PM_{2.5}$ and eBC, using them as proxies for B_{scat} and B_{abs}, and observing that while the eBC decreases rapidly after its morning maxima during all seasons, the $PM_{2.5}$ is decreasing much more slowly, due to photochemical reactions leading to the growth of pre-existing particles (Baumgardner

ACPD
15, 12539–12582, 2015

et al., 2004) and to the secondary production of particles (e.g. de Gouw et al., 2008; Herndon et al., 2008). This illustrates that whereas the minima in SSA observed during the morning are being driven by the presence of particles with eBC, the afternoon SSA is being driven mainly by changes in non-absorbing particles represented by B_{scat}.

3.3 Correlations and causal links between co-pollutants

The potential relationships between co-pollutants can be deduced by comparing the hourly trends in Figs. 6, 7 and 9. These links are further investigated by calculating the cross-correlations to highlight the temporal shifts that may change with season and offer additional evidence of how photochemical and thermodynamic processes drive the daily trends in gas concentrations and particle properties.

Figures 10–12 are correlations between pairs of pollutants as a function of the lag time that is varied from −10 h to +10 h, in 10 min increments. The vertical black dashed line is drawn at a zero lag time and the horizontal black dashed line is drawn at the crossover point from positive to negative correlation. The colors of the lines denote the season using the same coding as previous figures. Figure 10a illustrates the relationship between CO and NO_x and indicates that these two pollutants are highly correlated (R = 0.9) with no lag time, i.e. they are being produced at the same time and likely by the same source. The correlation between O_3 and NO_x (Fig. 10b), shows that their highest correlations are at lag times of −8, −7.5 and −7 h, for the warm-dry, cold-dry and rainy seasons, respectively. The maximum correlation at negative lag indicates that O_3 is linked to NO_x that was formed approximately eight hours earlier, as expected. These lag times are just another way of quantifying the time differences between the peaks in NO_x and O_3 that were seen in Fig. 6b and c. The one hour difference between the cold-dry and warm-dry seasons is caused by the change in DST as was explained earlier in the daily trends.

There is additional information contained in these cross-correlations by evaluating the time from maximum to zero correlation. This time, when the correlation coefficient crosses the zero point, is a measure of a characteristic parameter, referred to as the

ACPD
15, 12539–12582, 2015

integral time scale that is related to the rate at which the atmospheric processes produce, dilute or remove the pollutants. This integral time scale indicates how quickly the two pollutants are being de-correlated by dilution and mixing with other atmospheric components. For example, there is a single, season-independent integral time scale for the CO and NO_x correlation of 4–5 h whereas for the O_3 and NO_x there are three: 5, 4.5 and 4 h, respectively, for the cold-dry, warm-dry and rainy seasons. The effect of the change in DST is seen in the one hour difference in the cold and warm seasons.

The eBC and CO concentrations are highly correlated ($R > 0.8$) with no lag as seen in Fig. 11a, indicating that their sources are located in the same region. The high correlation between CO and BC mass (derived by an alternative method) in Mexico City was already pointed out by Baumgardner et al. (2000). The integral time scales are 6, 7 and 8.5 h during the warm-dry, rainy and dry-cold season, respectively.

The cross-correlation between the eBC and $PM_{2.5}$ (Fig. 11b) presents a more complicated picture that is related to the complex relationships between the two properties of particles: black carbon, a primary emission and particle mass, produced by a mixture of primary and secondary processes. Looking at the average maximum values of these two particle metrics in Table 2, we see that eBC is approximately 20 % of the mass of $PM_{2.5}$. Hence, the good correlation at zero lag for all seasons represents the fraction of the $PM_{2.5}$ that is eBC. The trends in the correlation coefficients rapidly diverge as the lag time increases. This reflects the secondary processes that either produce new particles or lead to the increase in mass of existing particles. These secondary processes can be aqueous, photochemical or a combination of both so the rate at which particles grow will depend on the temperature, relative humidity, pH and UV radiation flux. Since BC is a primary particle onto which organics, sulfates or nitrates can condense, there will remain a correlation between BC and $PM_{2.5}$. As the BC particle evolves and takes on a coating or mixture of other substances, when it is measured by the PAX it will continue to absorb energy and be identified as eBC, i.e. there is still a "memory" of the original particles that are being emitted even over very long lag times. As Fig. 11b illustrates the integral time scales exceed 10 h during all seasons. The much larger

ACPD
15, 12539–12582, 2015

integral time scale of the rainy season is most likely due to the higher humidity during this period that promotes aqueous phase reactions and particle growth. During the dry seasons, the secondary processes are only related to photochemical reactions. These are purely speculative, without corroboration using a chemical growth model, which is beyond the scope of this current study.

The correlations between the particle optical properties (B_{scat} and SSA) and the eBC and $PM_{2.5}$ are displayed in Fig. 12a and b. The relationship between B_{scat} and $PM_{2.5}$ that was discussed previously is highlighted in Fig. 13a, showing a correlation coefficient > 0.8 at zero lag time. The very long integral time scale is connected to the same secondary processes that led to the greater than 10 h time scales for the eBC and $PM_{2.5}$ (Fig. 11b). Figure 12b underscores the earlier discussion about the sensitivity of the SSA to eBC. The negative correlation is due to the inverse relationship between SSA and eBC. The correlations are higher in the dry months than in the rainy season because of the additional contribution of light scattering particles formed under conditions of high humidity. The separation in the integral time scales is also linked to the relative rate by which the B_{scat} increases as secondary processes promote particle growth in the different seasons.

4 Summary and conclusions

Measurements of SLCPs and precursor gases, made over a 13 month period from 6 March 2013 to 31 March 2014 have been evaluated to document and explain the seasonal trends related to changes in meteorology and radiative fluxes. The SLCPs that were analyzed are the eBC, O_3 and $PM_{2.5}$ and the co-pollutant gases of CO and NO_x. The eBC data are the longest, continuous measurements that have been conducted in Mexico City to date. These data extend over the three, primary seasons in Mexico City, i.e. rainy, cold-dry and warm-dry, and provide the basis for linking daily trends to the underlying physico-chemical processes that drive them.

ACPD
15, 12539–12582, 2015

The maximum concentrations of the gases, eBC and $PM_{2.5}$ were significantly less in the rainy season compared to the dry seasons. The maximum eBC changed from 8.8 to 13.1 $\mu g\,m^{-3}$ (44 %), (eBC), $PM_{2.5}$ from 49 to 73 $\mu g\,m^{-3}$ (61 %), NO_x from 144 to 252 ppm (78 %), O_3 from 73 to 100 ppb (51 %) and CO from 2.5 to 3.8 ppm (75 %). The primary factor that leads to lower concentrations in the rainy season is morning cloud formation that produces vigorous vertical motions and results in the dilution of all the pollutants. The clouds also reduce solar energy (UV radiation) and decrease the photochemical reactions that produce ozone and secondary aerosol particles.

A "weekend effect" is observed that is linked to changes in traffic patterns and the type of fuel burned. Significant decreases (t test) are observed between workdays (Monday through Saturday) and Sundays in the concentrations of CO, NO_x, eBC and $PM_{2.5}$. This decrease is most likely a result of reduced emissions by diesel burning vehicles. A significant increase is seen in the SSA because of its sensitivity and inverse relationship to changes in the light absorbing eBC. A significant effect was also seen in O_3 concentrations that did not change from workday to Sunday because of decreased production from VOCs was balanced by decreased inhibition by NO_x.

Cross correlations and the derived integral time scales were calculated between the co-pollutants in order to establish the temporal links and de-correlation times. Shorter integral time scales are related to rapid vertical mixing that erodes the "memory" of the pollutants that are originally coupled to the same source or location where they are produced. Cross correlations between pollutants where one or both can be affected by secondary chemical reactions typically have much longer integral time scales since these secondary reactions extend the memory of the coupled co-pollutants.

The maximum concentrations of eBC measured in 2000 (Baumgardner et al., 2002) and 2006 (Marley et al., 2009a, b), were 9.1 and 9.4 $\mu g\,m^{-3}$, respectively, compared to 8.8 and 13.1 $\mu g\,m^{-3}$ in the wet and dry seasons between March 2013 and March 2014. This shows that there has been no significant change in the eBC emissions over a 14 year period and suggests that the current pollution mitigation strategy will need

ACPD
15, 12539–12582, 2015

to be evaluated to develop new methods than can decrease potentially toxic levels of this particulate pollutant.

The results of this study are useful for clarifying the relationships between the co-pollutants of the SLCPs and identifying seasonal and workday/Sunday effects. The significant decrease in eBC on Sundays is linked to decreases in diesel combustion suggesting that eBC concentrations could be significantly reduced with tighter control of diesel consumption or regulations on diesel burning vehicles, providing a potential short-term solution for high concentrations and the related ill effects on the population.

Acknowledgements. We acknowledge Olivia Rivera-Hernández, Miguel Sánchez-Rodríguez and Alfonso López-Medina for providing criteria pollutants data and Angelica Neria-Hernández for her support of the PAX operation.

References

Arnott, W. P., Moosmüller, H., and Walker, J. W.: Nitrogen dioxide and kerosene-flame soot calibration of photoacoustic instruments for measurement of light absorption by aerosols, Rev. Sci. Instrum., 71, 4545–4552, 2000.

Arnott, W. P., Hamasha, K., Moosmüller, H., Sheridan, P. J., and Ogren, J. A.: Towards aerosol light-absorption measurements with a 7-wavelength aethalometer: evaluation with a photoacoustic instrument and 3-wavelength nephelometer, Aerosol Sci. Tech., 39, 17–29, 2005.

Arnott, W. P., Walker, J. W., Moosmüller, H., Elleman, R. A., Jonsson, H. H., Buzorius, G., Conant, W. C., Flagan, R. C., and Seinfeld, J. H.: Photoacoustic insight for aerosol light absorption aloft from meteorological aircraft and comparison with particle soot absorption photometer measurements: DOE Southern Great Plains climatic research facility and coastal stratocumulus imposed perturbation experiments, J. Geophys. Res., 111, D05S02, doi:10.1029/2005JD005964, 2006

Barth, M. C. and Church, A. T.: Regional and global distributions and lifetimes of sulfate aerosols from Mexico City and southeast China, J. Geophy. Res, 104, 30231–30239. 1999.

Baumgardner, D., Raga, G. B, Kok, G., Ogren, J., Rosas, I., Baez, A., and Novakov, T.: On the evolution of aerosol properties at a mountain site above Mexico City, J. Geophys. Res., 105, 22243–22253, 2000.

ACPD
15, 12539–12582, 2015

Baumgardner, D., Raga, G., Peralta, O., Rosas, I., Castro, T., Kuhlbusch, T., John, A., and Petzold, A.: Diagnosing black carbon trends in large urban areas using carbon monoxide measurements, J. Geophys. Res., 107, 8342, doi:10.1029/2001JD000626, 2002.
Baumgardner, D., Raga, G. B., and Muhlia, A.: Evidence for the formation of CCN by photochemical processes in Mexico City, Atmos. Environ., 38, 357–367, 2004.
Baumgardner, D., Kok, G. L., and Raga, G. B.: On the diurnal variability of particle properties related to light absorbing carbon in Mexico City, Atmos. Chem. Phys., 7, 2517–2526, doi:10.5194/acp-7-2517-2007, 2007.
Baumgardner, D., Grutter, M., Allan, J., Ochoa, C., Rappenglueck, B., Russell, L. M., and Arnott, P.: Physical and chemical properties of the regional mixed layer of Mexico's Megapolis, Atmos. Chem. Phys., 9, 5711–5727, doi:10.5194/acp-9-5711-2009, 2009.
Bond, T. C. and Bergstrom, R. W.: Light absorption by carbonaceous particles: an investigative review, Aerosol Sci. Tech., 40, 27–67, 2006.
Bond, T. C., Habib, G., and Bergstrom, R. W.: Limitations in the enhancement of visible light absorption due to mixing state, J. Geophys. Res., 111, D20, doi:10.1029/2006JD007315, 2006.
Bond, T. C., Doherty, S. J., Fahey, D. W., Forster, P. M., Berntsen, T., DeAngelo, B. J., Flanner, M. G., Ghan, S., Kärcher, B., Koch, D., Kinne, S., Kondo, Y., Quinn, P. K., Sarofim, M. C., Schultz, M. G., Schulz, M., Venkataraman, C., Zhang, H., Zhang, S., Bellouin, N., Guttikunda, S. K., Hopke, P. K., Jacobson, M. Z., Kaiser, J. W., Klimont, Z., Lohmann, U., Schwarz, J. P., Shindell, D., Storelvmo, T., Warren, S. G., and Zender, C. S.: Bounding the role of black carbon in the climate system: a scientific assessment, J. Geophys. Res.-Atmos., 118, 5380–5552, 2013.
Bowerman, N. H. A., Frame, D. J., Huntongford, C., Lowe, J. A., Smith, S. M. and Myles, A. R.: The role of short-lived climate pollutants in meeting temperature goals, Nat. Clim. Change, 3, 1021–1024, 2013.
Chan, T. W., Brook, J. R., Smallwood, G. J., and Lu, G.: Time-resolved measurements of black carbon light absorption enhancement in urban and near-urban locations of southern Ontario, Canada, Atmos. Chem. Phys., 11, 10407–10432, doi:10.5194/acp-11-10407-2011, 2011.
Collins, C. O. and Scott, S. L.: Air pollution in the valley of Mexico, Geogr. Rev., 2, 119–133, 1993.
de Gouw, J. A., Welsh-Bon, D., Warneke, C., Kuster, W. C., Alexander, L., Baker, A. K., Beyersdorf, A. J., Blake, D. R., Canagaratna, M., Celada, A. T., Huey, L. G., Junkermann, W.,

ACPD
15, 12539–12582, 2015

Onasch, T. B., Salcido, A., Sjostedt, S. J., Sullivan, A. P., Tanner, D. J., Vargas, O., Weber, R. J., Worsnop, D. R., Yu, X. Y., and Zaveri, R.: Emission and chemistry of organic carbon in the gas and aerosol phase at a sub-urban site near Mexico City in March 2006 during the MILAGRO study, Atmos. Chem. Phys., 9, 3425–3442, doi:10.5194/acp-9-3425-2009, 2009.

Edgerton, S. A., Arriaga, J. L., Archuleta, J., Bian, X., Bossert, J. E., Chow, J. C., Coulter, R. L., Doran, J. C., Doskey, P. V., Elliot, S., Fast, J. D., Gaffney, J. S., Guzman, F., Hubbe, J. M., Lee, J. T., Malone, E. L., Marley, N. A., McNair, L. A., Neff, W., Ortiz, E., Petty, R., Ruiz, M., Shaw, W. J., Sosa, G., Vega, E., Watson, J. G., Whiteman, C. D., and Zhong, S.: Particulate air pollution in Mexico City: a collaborative research project, J. Air Waste Manage., 49, 1221–1229, 1999.

Herndon, S. C., Onasch, T. B., Wood, E. C., Kroll, J. H., Canagaratna, M. R., Jayne, J. T., Zavala, M. A., Knighton, W. B., Mazzoleni, C., Dubey, M. K., Ulbrich, I. M., Jimenez, J. L., Seila, R. de Gouw, J. A., de Foy, B., Fast, J., Molina, L. T., Kolb, C. E., and Worsnop, D. R.: The correlation of secondary organic aerosol with odd oxygen in a megacity outflow, Geophys. Res. Lett., 35, L15804, doi:10.1029/2008GL034058, 2008.

Holder, A. L., Hagler, G. S. W., Yelverton, T. L. B., and Hays, M. D.: On-road black carbon instrument intercomparison and aerosol characteristics by driving environment, Atmos. Environ., 88, 183–191, 2014.

Jauregui, E.: Mesomicroclima de la Ciudad de México, Instituto de Geografía, UNAM, Mexico City, Mexico, 87 pp., 1971.

Jiang, M., Marr, L. C., Dunlea, E. J., Herndon, S. C., Jayne, J. T., Kolb, C. E., Knighton, W. B., Rogers, T. M., Zavala, M., Molina, L. T., and Molina, M. J.: Vehicle fleet emissions of black carbon, polycyclic aromatic hydrocarbons, and other pollutants measured by a mobile laboratory in Mexico City, Atmos. Chem. Phys., 5, 3377–3387, doi:10.5194/acp-5-3377-2005, 2005.

Johnson, K. S., Zuberi, B., Molina, L. T., Molina, M. J., Iedema, M. J., Cowin, J. P., Gaspar, D. J., Wang, C., and Laskin, A.: Processing of soot in an urban environment: case study from the Mexico City Metropolitan Area, Atmos. Chem. Phys., 5, 3033–3043, doi:10.5194/acp-5-3033-2005, 2005.

Lewis, K. A., Arnott, W. P., Moosmüller, H., Chakrabarty, R. K., Carrico, C. M., Kreidenweis, S. M., Day, D. E., Malm, W. C., Laskin, A., Jimenez, J. L., Ulbrich, I. M., Huffman, J. A., Onasch, T. B., Trimborn, A., Liu, L., and Mishchenko, M. I.: Reduction in biomass burning

ACPD
15, 12539–12582, 2015

aerosol light absorption upon humidification: roles of inorganically-induced hygroscopicity, particle collapse, and photoacoustic heat and mass transfer, Atmos. Chem. Phys., 9, 8949–8966, doi:10.5194/acp-9-8949-2009, 2009.

Liu, S., Aiken, A. C., Arata, C., Dubey, M. K., Stockwell, C. E., Yokelson, R. J., Stone, E. A., Jayarathne, T., Robinson, A. L., DeMott, P. J., and Kreidenweis, S. M.: Aerosol single scattering albedo dependence on biomass combustion efficiency: laboratory and field studies, Geophys. Res. Lett., 41, 742–748, 2014.

Marley, N. A., Gaffney, J. S., Ramos-Villegas, R., and Cárdenas González, B.: Comparison of measurements of peroxyacyl nitrates and primary carbonaceous aerosol concentrations in Mexico City determined in 1997 and 2003, Atmos. Chem. Phys., 7, 2277–2285, doi:10.5194/acp-7-2277-2007, 2007.

Marley, N. A., Gaffney, J. S., Tackett, M., Sturchio, N. C., Heraty, L., Martinez, N., Hardy, K. D., Marchany-Rivera, A., Guilderson, T., MacMillan, A., and Steelman, K.: The impact of biogenic carbon sources on aerosol absorption in Mexico City, Atmos. Chem. Phys., 9, 1537–1549, doi:10.5194/acp-9-1537-2009, 2009a.

Marley, N. A., Gaffney, J. S., Castro, T., Salcido, A., and Frederick, J.: Measurements of aerosol absorption and scattering in the Mexico City Metropolitan Area during the MILAGRO field campaign: a comparison of results from the T0 and T1 sites, Atmos. Chem. Phys., 9, 189–206, doi:10.5194/acp-9-189-2009, 2009b.

Molina, L. T., Kolb, C. E., de Foy, B., Lamb, B. K., Brune, W. H., Jimenez, J. L., Ramos-Villegas, R., Sarmiento, J., Paramo-Figueroa, V. H., Cardenas, B., Gutierrez-Avedoy, V., and Molina, M. J.: Air quality in North America's most populous city – overview of the MCMA-2003 campaign, Atmos. Chem. Phys., 7, 2447–2473, doi:10.5194/acp-7-2447-2007, 2007.

Molina, L. T., Madronich, S., Gaffney, J. S., Apel, E., de Foy, B., Fast, J., Ferrare, R., Herndon, S., Jimenez, J. L., Lamb, B., Osornio-Vargas, A. R., Russell, P., Schauer, J. J., Stevens, P. S., Volkamer, R., and Zavala, M.: An overview of the MILAGRO 2006 Campaign: Mexico City emissions and their transport and transformation, Atmos. Chem. Phys., 10, 8697–8760, doi:10.5194/acp-10-8697-2010, 2010.

Moosmüller, H., Chakrabarty, R. K., and Arnott, W. P.: Aerosol light absorption and its measurement: a review, J. Quant. Spectrosc. Ra., 110, 844–878, 2009.

Murphy, D.: The effect of water evaporation on photoacoustic signals in transition and molecular flow, Aerosol Sci. Tech., 43, 356–364, 2009.

ACPD
15, 12539–12582, 2015

Nakayama, T., Suzuki, H., Kagamitani, S., Ikeda, Y., Uchiyama, A., and Matsumi, Y.: Characterization of a three wavelength photoacoustic soot spectrometer (PASS-3) and photoacoustic extinctiometer (PAX), J. Meteorol. Soc. Jpn., 93, doi:10.2151/jmsj.2015-016, 2015.

Pérez Vidal, H. and Raga, G. B.: On the vertical distribution of pollutants in Mexico City, Atmósfera, 11, 95–108, 1998.

Petzold, A., Ogren, J. A., Fiebig, M., Laj, P., Li, S.-M., Baltensperger, U., Holzer-Popp, T., Kinne, S., Pappalardo, G., Sugimoto, N., Wehrli, C., Wiedensohler, A., and Zhang, X.-Y.: Recommendations for reporting "black carbon" measurements, Atmos. Chem. Phys., 13, 8365–8379, doi:10.5194/acp-13-8365-2013, 2013.

Schifter, I., Díaz, L., Durán, J., Guzmán, E., Chávez, O., and López-Salinas, E.: Remote sensing study of emissions from motor vehicles in the metropolitan area of Mexico City, Environ. Sci. Technol., 37, 395–401, 2003.

Shindell, D., Kuylenstierna, J. C. I., Vignati, E., van Dingenen, R., Amann, M., Klimont, Z., Anenberg, S. C., Muller, N., Janssens-Maenhout, G., Raes, F., Schwartz, J., Faluvegi, G., Pozzoli, L., Kupiainen, K., Höglund-Isaksson, L., Emberson, L., Streets, D., Ramanathan, V., Hicks, K., Kim Oanh, N. T., Milly, G., Williams, M., Demkine, V., and Fowler, D.: Simultaneously mitigating near-term climate change and improving human health and food security, Science, 335, 183–189, 2012.

Singh, H. B., Brune, W. H., Crawford, J. H., Flocke, F., and Jacob, D. J.: Chemistry and transport of pollution over the Gulf of Mexico and the Pacific: spring 2006 INTEX-B campaign overview and first results, Atmos. Chem. Phys., 9, 2301–2318, doi:10.5194/acp-9-2301-2009, 2009.

SMA-GDF (Secretaria del Medio Ambiente del Gobierno del Distrito Federal): Inventario de emisiones contaminantes y de efecto invernadero el año de 2012 de la Zona Metropolitana del Valle de México, Secretaría del Medio Ambiente, Gobierno de México, México, available at: http://www.aire.df.gob.mx/ (last access: 28 April 2015), 2012.

Stephens, S., Madronich, S., Wu, F., Olson, J. B., Ramos, R., Retama, A., and Muñoz, R.: Weekly patterns of México City's surface concentrations of CO, NO_x, PM_{10} and O_3 during 1986–2007, Atmos. Chem. Phys., 8, 5313–5325, doi:10.5194/acp-8-5313-2008, 2008.

Stull, R.: An Introduction to Boundary Layer Meteorology, Atmospheric and Oceanographic Library, vol. 13, Springer, New York, NY, 670 pp., 1988.

Subramanian, R., Kok, G. L., Baumgardner, D., Clarke, A., Shinozuka, Y., Campos, T. L., Heizer, C. G., Stephens, B. B., de Foy, B., Voss, P. B., and Zaveri, R. A.: Black carbon over

ACPD
15, 12539–12582, 2015

Mexico: the effect of atmospheric transport on mixing state, mass absorption cross-section, and BC/CO ratios, Atmos. Chem. Phys., 10, 219–237, doi:10.5194/acp-10-219-2010, 2010.

ACPD
15, 12539–12582, 2015

Table 1. Daily and seasonal statistics.

Parameter	Statistic	Rainy Workdays	Rainy Sundays	Cold Dry Workdays	Cold Dry Sundays	Warm Dry Workdays	Warm Dry Sundays
CO (ppm)	Average	0.64	0.47	0.83	0.69	0.71	0.57
	Median	0.50	0.40	0.60	0.50	0.47	0.40
	Q75	0.88	0.60	1.06	0.94	0.84	0.72
	Q95	1.70	1.00	2.30	1.70	2.22	1.56
	Maxima	2.51	1.70	3.99	3.52	3.63	2.35
O_3 (ppb)	Average	19	23	22	25	37	42
	Median	9	13	8	12	25	29
	Q75	29	33	35	39	64	74
	Q95	71	71	86	87	120	117
	Maxima	73	74	83	89	117	122
NO_x (ppb)	Average	62	45	82	67	87	69
	Median	58	39	88	69	75	53
	Q75	46	34	61	52	46	36
	Q95	74	52	112	92	92	66
	Maxima	144	86	252	179	251	157
$PM_{2.5}$ $\mu g\,m^{-3}$	Average	24	19	38	31	45	44
	Median	21	18	35	29	44	44
	Q75	31	24	48	39	59	51
	Q95	52	40	70	60	81	72
	Maxima	49	39	67	56	78	71
eBC $\mu g\,m^{-3}$	Average	2.3	1.0	3.1	1.7	2.5	1.3
	Median	1.8	0.8	2.2	1.3	1.7	1.1
	Q75	3.1	1.4	4.1	2.7	3.1	1.7
	Q95	5.9	2.7	9.2	4.5	7.7	3.5
	Maxima	8.8	6.1	13.7	8.7	12.5	5.5
SSA	Average	0.74	0.83	0.72	0.78	0.78	0.89
	Median	0.78	0.89	0.74	0.81	0.82	0.92
	Q75	0.86	0.96	0.83	0.89	0.88	0.94
	Q95	0.99	1.00	0.93	1.00	0.94	1.00
	Maxima	1.00	1.00	1.00	1.00	1.00	1.00
B_{scat}	Average	34	27	37	32	43	51
	Median	27	21	31	24	35	45
	Q75	43	34	48	37	58	65
	Q95	82	71	84	71	92	106
	Maxima	100	82	98	102	104	113

ACPD
15, 12539–12582, 2015

Table 2. Daily and seasonal maxima.
No underline = not significant; underline, no bold numbers = significant decrease from Monday–Saturday to Sunday; underline, bold numbers = significant increase from Monday–Saturday to Sunday; underline, italics = significant decrease between seasons; underline, bold italics = significant increase between seasons.

Parameter	Day of the week	Rainy Maximum (Std. – %)	Cold-Dry Maximum (Std. – %)	Warm-Dry Maximum (Std. – %)	Rainy to Cold % difference (*T* test Values)	Rainy to Warm % difference (*T* test Values)	Cold to Warm % difference (*T* test Values)
CO (ppm)	Monday–Saturday	2.5 (55)	4.0 (64)	3.6 (55)	***44 (4.8)***	***37 (3.2)***	8 (−0.8)
	Sunday	1.7 (25)	3.5 (68)	2.4 (47)	***75 (3.6)***	***36 (1.7)***	*−41 (−1.8)*
O_3 (ppb)	Monday–Saturday	73 (38)	83 (37)	117 (29)	***13 (2.7)***	***47 (8)***	***35 (6.2)***
	Sunday	74 (35)	89 (31)	122 (14)	***19 (1.8)***	***51 (5.6)***	***33 (3.9)***
NO_x (ppb)	Monday–Saturday	144 (41)	252(41)	251(43)	***53 (10.1)***	***52 (6.1)***	−1 (−0.1)
	Sunday	86 (25)	179 (45)	157 (48)	***78 (5.9)***	***50 (2.2)***	−30 (1.6)
$PM_{2.5}$ $\mu g\,m^{-3}$	Monday–Saturday	49 (37)	67 (31)	78 (32)	***34 (7.7)***	***47 (7.4)***	***14 (2.5)***
	Sunday	39 (39)	56 (34)	71 (18)	***37 (3.3)***	***61 (5.4)***	***26 (2.5)***
eBC $\mu g\,m^{-3}$	Monday–Saturday	8.8 (44)	13.7 (47)	12.5 (55)	***44 (7.7)***	***36 (3)***	−9 (−0.9)
	Sunday	6.1 (100)	8.7 (70)	5.5 (59)	36 (1.5)	−10 (−0.2)	−45 (−1.5)
SSA	Monday–Saturday	0.74 (16)	0.71 (15)	0.77 (12)	*−4 (−2)*	4 (1.4)	***9 (2.9)***
	Sunday	**0.83 (13)**	**0.77 (15)**	**0.89 (5)**	*−7 (−1.7)*	***7 (1.7)***	***15 (3.4)***
B_{scat} Mm^{-1}	Monday–Saturday	100 (46)	98 (45)	104 (40)	−3 (−0.5)	4 (0.5)	7 (0.9)
	Sunday	82 (48)	102 (68)	113 (22)	23 (1.3)	***33 (2.1)***	10 (0.6)

ACPD
15, 12539–12582, 2015

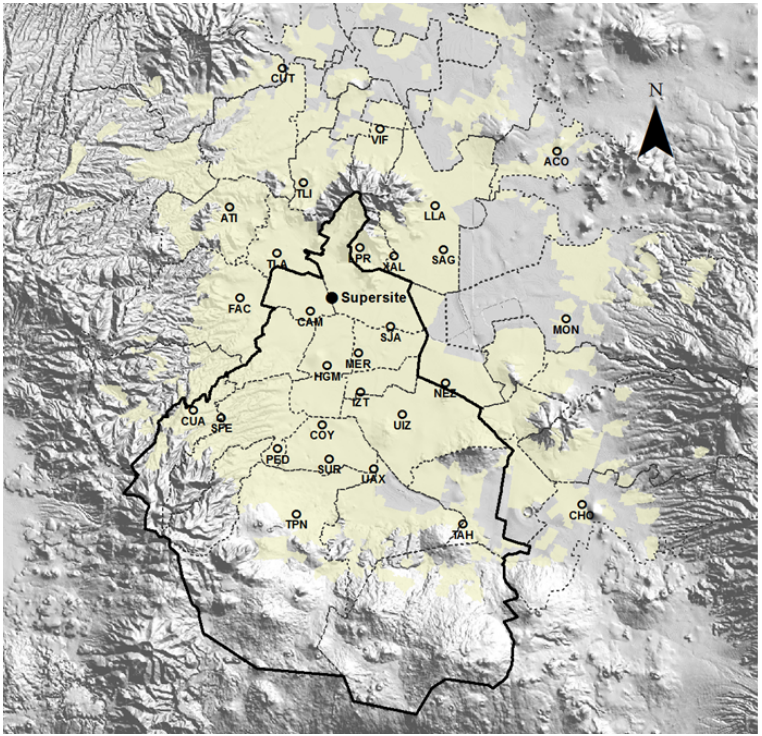

Figure 1. This map of the Metropolitan Area of Mexico City shows the locations of the RAMA air quality monitoring stations and the location of the supersite where the measurements were made for this paper. Map courtesy of the Mexico City government (http://www.aire.df.gob.mx/default.php).

ACPD
15, 12539–12582, 2015

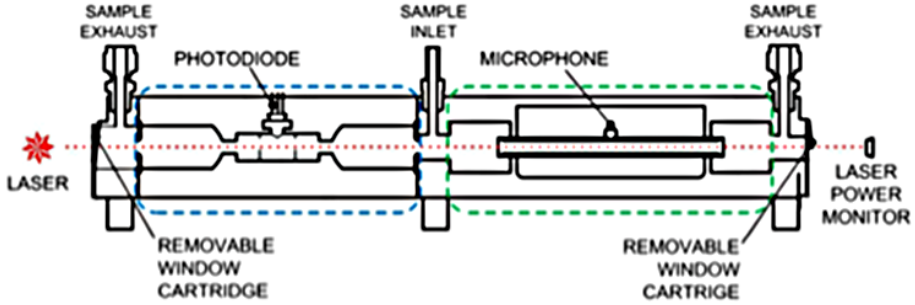

Figure 2. Diagram showing the scattering (blue dashed region) and absorption (green dashed region) cells in the photoacoustic extinctiometer (PAX).

ACPD
15, 12539–12582, 2015

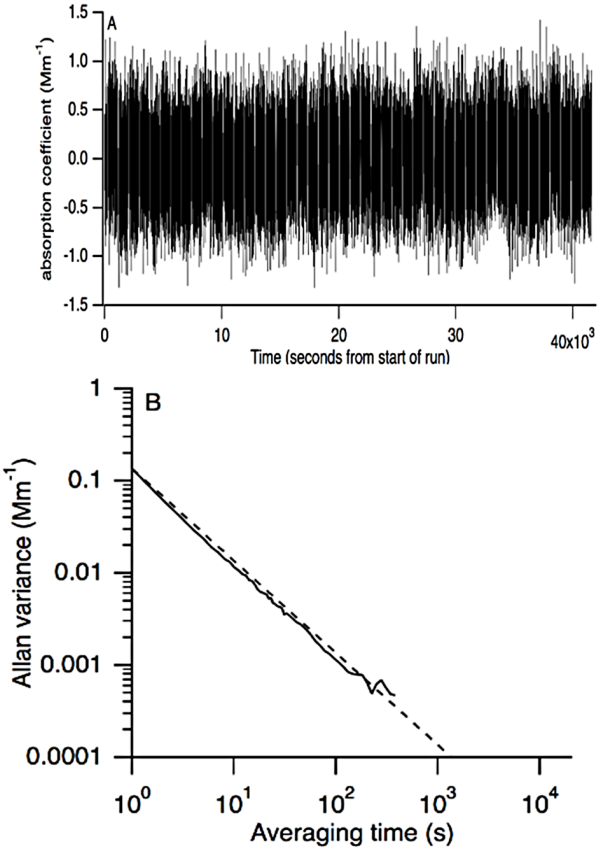

Figure 3. Background-corrected absorption coefficients **(a)** and Allan variance **(b)** measured by an 870 nm PAX sampling filtered laboratory air overnight in a temperature-controlled environment. The dashed line in **(b)** gives the variance for white noise.

ACPD
15, 12539–12582, 2015

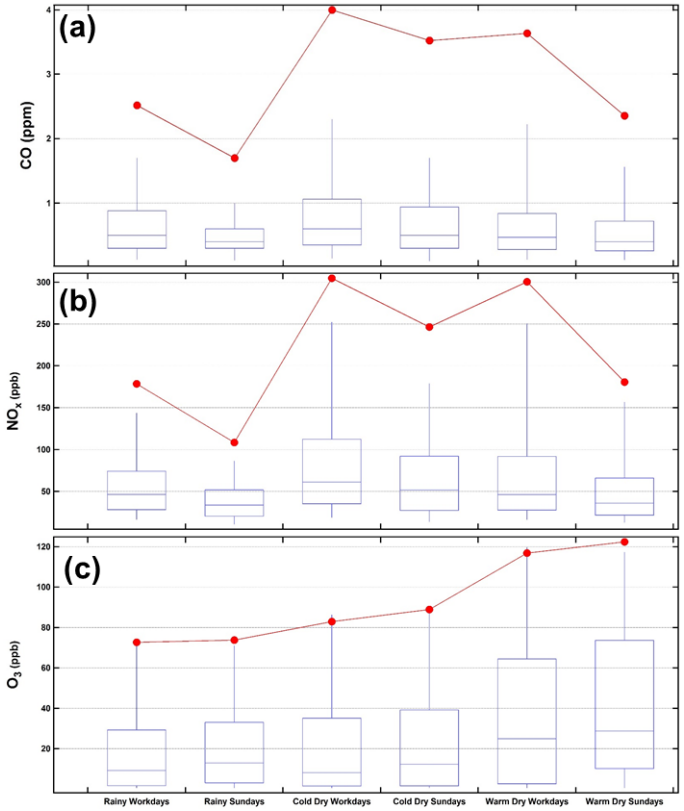

Figure 4. The box and whisker plots show median (horizontal line within the box), 25 % quantile (bottom of box), 75 % quantile (top of box), 5 % quantile (bottom whisker) and 95 % quantile (top whisker). In addition the average of the daily maxima are shown with the red, filled circles. The trends in these statistics as a function season, workdays and Sundays are plotted for **(a)** CO, **(b)** NO_x and **(c)** O_3.

ACPD
15, 12539–12582, 2015

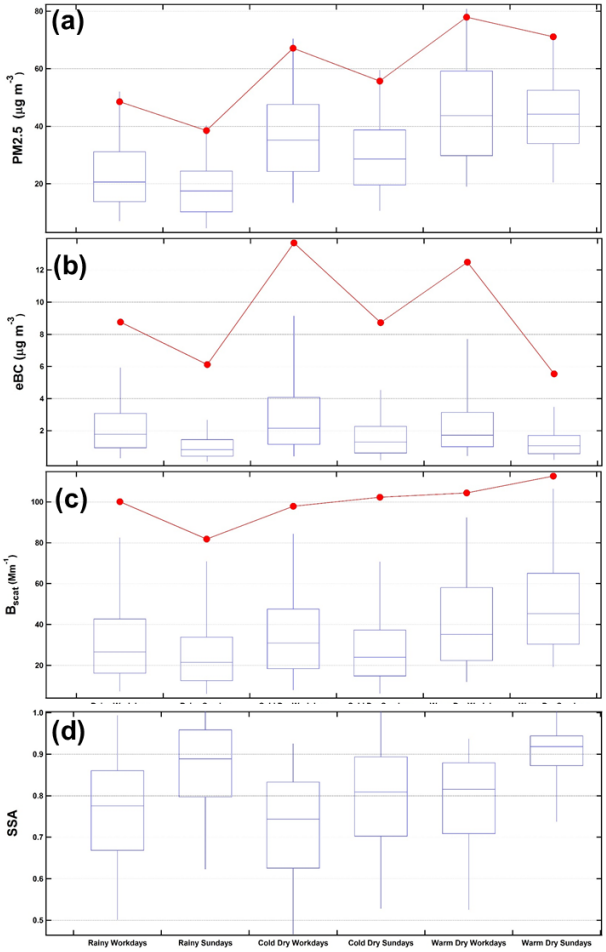

Figure 5. The same as Fig. 4 but for **(a)** $PM_{2.5}$, **(b)** eBC, **(c)** B_{scat} and **(d)** SSA.

ACPD
15, 12539–12582, 2015

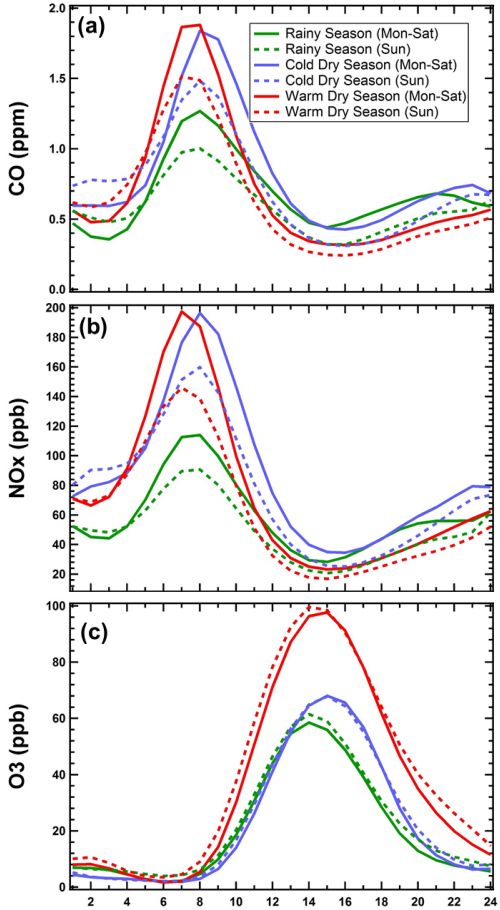

Figure 6. The average hourly values are shown separated by workday (solid) and weekend (dashed) and by season: warm-dry (red), rainy (green) and cold-dry (blue) for **(a)** CO, **(b)** NO_x and **(c)** O_3 concentrations.

ACPD
15, 12539–12582, 2015

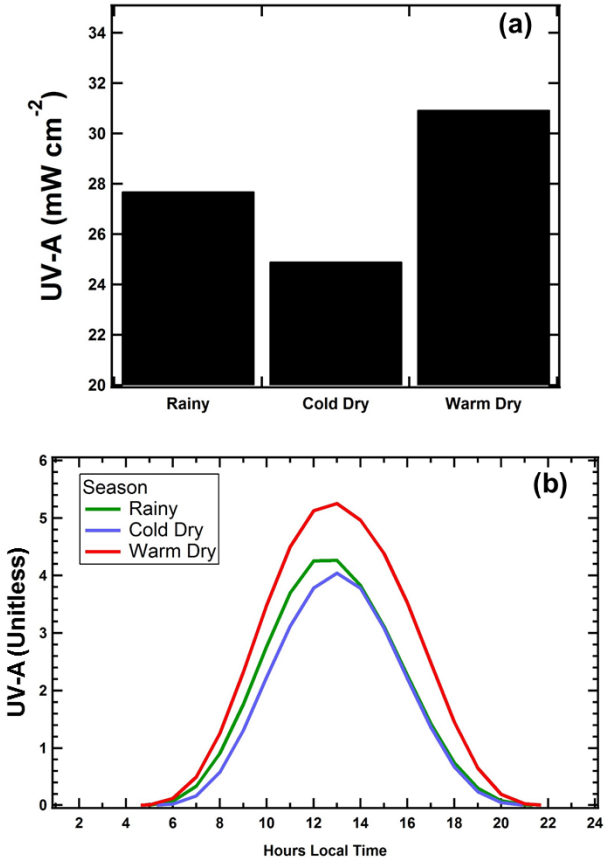

Figure 7. (a) The average, daily accumulated UV-A is shown in the bar chart illustrating the impact of clouds during the rainy season when the sun reaches its maximum elevation angle at the Mexico City latitude. **(b)** The average hourly and seasonal UV-A exposure.

ACPD
15, 12539–12582, 2015

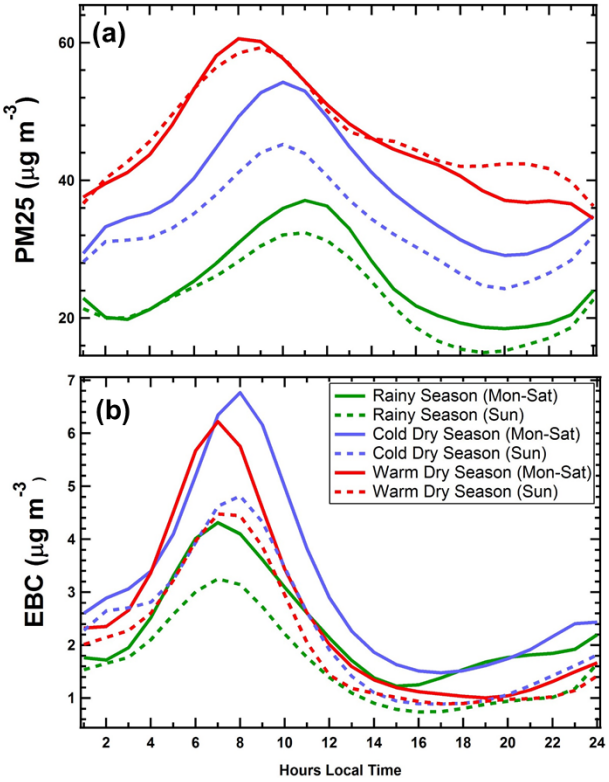

Figure 8. As in Fig. 6, the average hourly **(a)** $PM_{2.5}$ mass and **(b)** eqivalent black carbon concentrations are shown differentiated by seasons and day of the week.

ACPD
15, 12539–12582, 2015

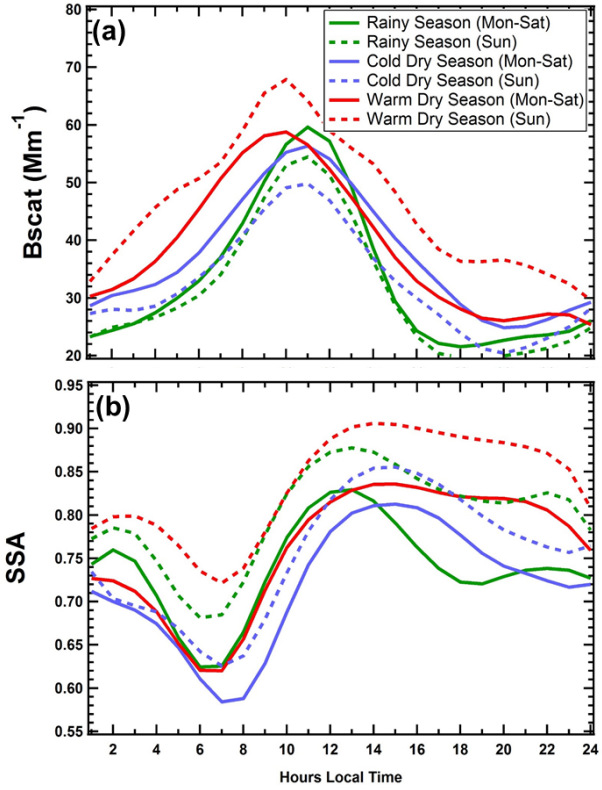

Figure 9. As in Figs. 6 and 8 but for **(a)** light scattering coefficient, B_{scat} and **(b)** single scattering albedo, SSA.

ACPD
15, 12539–12582, 2015

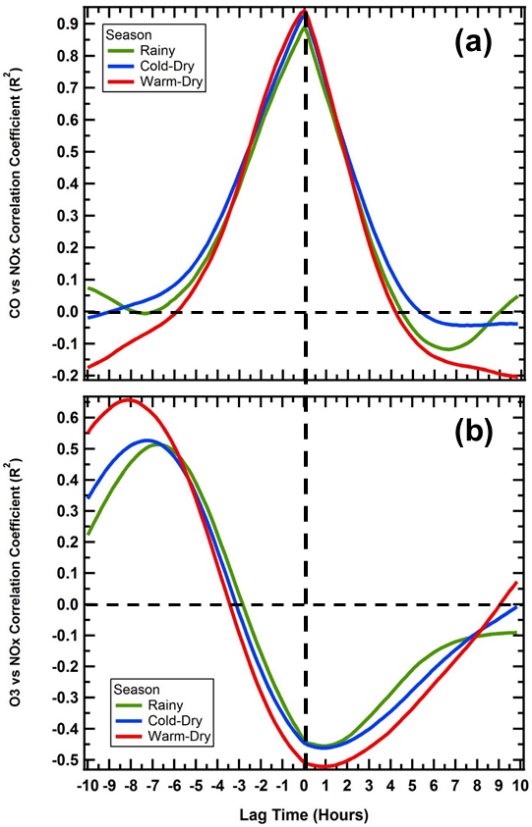

Figure 10. These plots illustrate the correlations between **(a)** CO and NO_x, **(b)**, O_3 and NO_x as a function of the lag time and differentiated by season. The vertical dashed line shows the correlation of the parameters at no lag time. The horizontal dashed line demarks the cross over from positive to negative correlation. The lag time was varied in 10 min intervals.

ACPD
15, 12539–12582, 2015

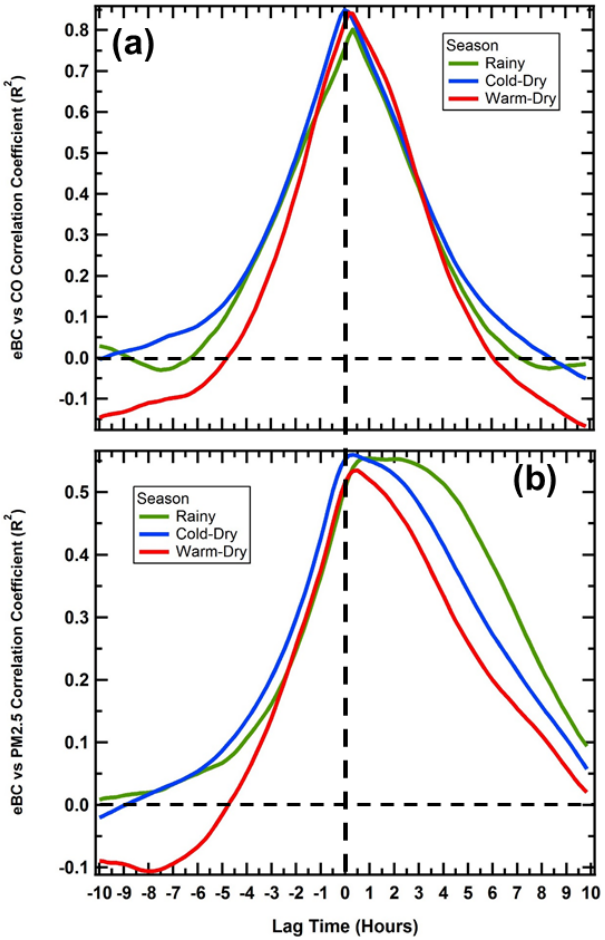

Figure 11. As in Fig. 10, these plots illustrate the correlations between **(a)** eBC and CO, **(b)**, eBC and $PM_{2.5}$ as a function of the lag time and differentiated by season.

ACPD
15, 12539–12582, 2015

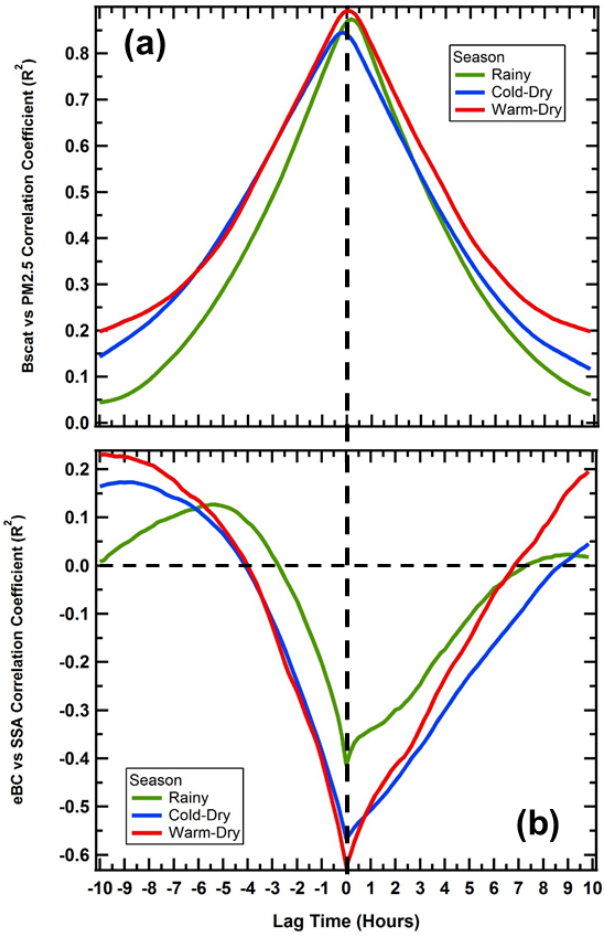

Figure 12. As in Fig. 10, these plots illustrate the correlations between **(a)** Bscat and $PM_{2.5}$, **(b)**, eBC and SSA as a function of the lag time and differentiated by season.

ACPD
15, 12539–12582, 2015